Temporal Non-Uniform Compressive Sampling for Dynamic Optical Coherence Tomography

AMY L. OLDENBURG,[1,2,*] PAN JI,[1] XIAO YU,[2] AND LIN YANG[1]

[1]*Department of Physics and Astronomy, University of North Carolina at Chapel Hill, Chapel Hill, NC 27599-3255, USA*
[2]*Biomedical Research Imaging Center University of North Carolina at Chapel Hill, Chapel Hill, NC 27599-7513, USA*
**aold@physics.unc.edu*

Abstract: Optical coherence tomography (OCT) has great utility for capturing dynamic processes, but such applications are particularly data intensive. Samples such as biological tissues exhibit temporal features at varying time scales, which makes data reduction challenging. Here we propose a method for capturing short- and long-time correlations of a sample using temporally compressive sampling to reduce scan time and memory overhead. The proposed method involves non-uniform sampling in time to separate the relative contributions of white noise, fluctuating features, and stationary features. This approach is demonstrated on mammary epithelial cell spheroids in 3D culture for capturing intracellular motility without loss of signal integrity. Results show that the spatial patterns of motility are preserved and that hypothesis tests of spheroids treated with blebbistatin, a motor protein inhibitor, are unchanged with up to 8-fold compression. In broader contexts, the ability to measure short- and long-time correlations compressively will enable new applications in (3+1)D imaging and high-throughput screening.

1. Introduction

By merit of its high speed and depth resolution, OCT has become a powerful tool for imaging dynamic processes such as diffusion [1], flow [2], and cellular processes [3]. A key challenge in dynamic OCT imaging is separating features with different temporal dynamics. For example, blood flow detection can be improved by separating bulk motion using a split spectrum analysis technique [4]. One can distinguish cellular responses to different drugs by extracting features from speckle fluctuation spectra, as shown using a related low-coherence imaging technique [5]. In OCT studies of ciliated tissues, one is interested in assessing the ciliary beat frequency [6, 7]. Or, one might measure the diffusion rate of nanoparticles with OCT to image differences in tissue nanoporosity [8]. Often times it is desired to contrast these dynamic features volumetrically, such as for quantitative retinal blood flow imaging [9], airway tissue surface dynamics [10], and imaging of organoid motility [11], which require high dimensional (3+1)D imaging. Even if only cross-sectional (2+1)D imaging is needed, screening applications such as personalizing cancer chemotherapies [12] and toxicant assays [13] require additional dimensions of study conditions. The development of compressive sampling techniques would be beneficial for reducing OCT scanning requirements and memory overhead, and favorable toward such high-throughput applications. While prior efforts have made progress in this regard using traditional "compressed sensing" (CS) methods in space [14], here we introduce a compressive sampling method (that is not based upon CS theory) along the temporal (1D) dimension in such a way that the temporal features of interest are preserved. In order to accomplish this, we propose a non-uniform compressive sampling method (NUCS) that estimates both short- and long-time correlations of the sample, and yields accurate signal estimates at each point in space from highly under-sampled measurements. In comparison, uniform temporally compressive sampling has been proposed [15] with some success and compatibility with scanning protocols that can be implemented in hardware; however simply reducing the sampling rate loses the ability to capture short-time correlations accurately. Non-uniform compressive sampling was notably proposed in the context of velocimetry [16], but

the scheme employed a random selection of time points that is not readily implemented in hardware, and was optimized solely for flow estimation. As shown below, the NUCS method proposed here strikes a balance between accurate estimation of both short- and long-time correlations, while employing a regular sampling pattern that is readily implemented in hardware.

In this paper, we have framed the problem as that of estimating an OCT temporal autocorrelation-based motility metric, "motility amplitude" *M*, with temporal compressive sampling. The utility of *M* has been demonstrated in tracking the responses of human mammary epithelial cells in 3D cultures to drugs and toxicants [13, 17-19]. Below we describe how *M* quantifies the relative amplitude of fluctuations exhibiting short-time correlations that are distinct from white noise and from stationary features. Similar autocorrelation-based metrics for cellular motility contrast have been employed to assess corneal cross-linking [20] and urothelial cancer cell distribution [21]. Here our NUCS method is applied to estimating *M* from the magnitude of the OCT signal, avoiding the need for phase-resolved OCT. However, the proposed method may also be applicable for compressively sampling decorrelations in the complex OCT signal (see, *e.g*., [22] for a discussion of differences between amplitude and phase-resolved methods). As shown below, the proposed NUCS method provides better estimation than uniform sampling under the same compression ratio, with the possibility of viable compression ratios of up to 8, which may dramatically improve scan time and storage efficiency in high throughput experiments.

2. Background and Methods

2.1 Distinguishing dynamic processes in OCT

Consider the time-varying magnitude of the OCT signal, S_{OCT}, collected from a coherence volume in the single-scattering approximation. Within the coherence volume there may be multiple light scatterers that contribute to S_{OCT}, each moving with different velocities and different amounts of coordination. Let us consider collecting S_{OCT} with sampling time t_s over a total time t_{total}, then computing its temporal autocorrelation $\Gamma(t)$. An idealized autocorrelation trace is shown in Fig. 1a. The autocorrelation trace primarily reveals processes that cause S_{OCT} to fluctuate on a time scale longer than t_s, but shorter than t_{total}; we call the time scale of such processes the memory time of the "motile" scatterers, t_m. Slowly moving scatterers that do not change S_{OCT} over t_{total} give rise to the autocorrelation at t_{total}, $\Gamma(t_{total})$. If we assume these slowly moving scatterers are perfectly stationary, we may approximate $\Gamma(t_{total})$ as being equal to $\overline{S}_{OCT}{}^2$. Consider an OCT system that is limited by white noise (such as shot noise, which is the limiting type of noise in many OCT systems). Because white noise has infinite bandwidth, it decorrelates instantaneously. Thus, the portion of the autocorrelation that decorrelates between the first two samples, $\Gamma(0) - \Gamma(t_s)$, is imparted by white noise, and by any other processes causing fluctuations faster than t_s (*e.g*. extremely rapidly moving scatterers, as well as motile scatterers that exhibit a small amount of decorrelation over t_s.) In this picture, we can isolate the contribution of the motile scatterers approximately by $\Gamma(t_s) - \overline{S}_{OCT}{}^2$, *i.e*., the amount that the autocorrelation trace decays between t_s and t_{total}.

A few things should be noted at this stage. First, the difference $\Gamma - \overline{S}_{OCT}{}^2$ is equivalent to the autocovariance. For the purposes of discussion, here we chose to separate Γ (autocorrelation) and $\overline{S}_{OCT}{}^2$, which are impacted differently by different compression methods. Second, it may be possible to estimate the white noise contribution to $\Gamma(0)$ using methods described in [23], which could provide a better estimate of the motile scatterer contribution. However, these methods were unable to be implemented in this study, as they require an OCT system with certain noise statistics and a good estimate of the signal-to-noise ratio (SNR).

To validate the picture of Fig. 1a, example OCT data sets of mammary epithelial cell (MEC) spheroids in 3D culture under varying conditions were analyzed. MEC spheroids exhibit

intracellular motility (*i.e.*, in-place motions of sub-resolution, intracellular components) that decorrelate OCT signals with a 1/*e* decay time on the order of 5s [24]. Here we compared spheroids that were formalin fixed and expected to exhibit no motility, spheroids that were treated with blebbistatin, a myosin II inhibitor, for 6 days and expected to exhibit suppressed motility, and spheroids that were untreated for 2 days as an example of high motility. (A shorter culture time point of 2 days for the latter was chosen to avoid possible apoptosis). Pixelwise autocorrelation traces averaged over regions of the spheroids are displayed in Fig. 1b. All traces exhibit an initial decay at $\Gamma(t_s)$ between 2 – 7% of $\Gamma(0)$ attributed predominantly to white noise. The trace of the fixed spheroid exhibits negligible further decay, consistent with the picture that it is comprised of stationary scatterers. In contrast, the traces of the blebbistatin and control spheroids decay further, reaching stable values at ~30 s, suggesting they contain motile scatterers. The blebbistatin-treated spheroid exhibits a smaller proportion of decay compared to control, consistent with the expectation that it has suppressed motility (fewer and/or slower motile scatterers). In all cases, a significant fraction of the autocorrelation (between 83 – 99%) remains after t_{total} = 112s (not shown), which is attributed to stationary scatterers.

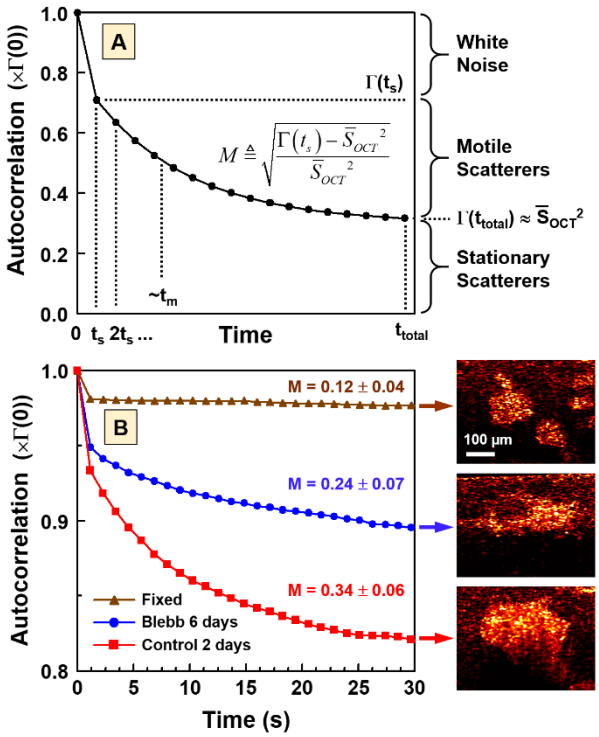

Fig. 1. Short- and long-time processes visualized by temporal autocorrelations of the OCT signal, S_{OCT}. Autocorrelations are displayed in units of $\Gamma(0)$. (A) Idealized autocorrelation showing relative contributions of white noise, motile scatterers with characteristic decay time t_m, and stationary scatterers. The motility amplitude, M, isolates the contribution of motile scatterers. (B) Example autocorrelations from OCT of spheroids with low M (formalin fixed), moderate M (blebbistatin treated) and high M (untreated).

To estimate the contribution of the motile scatterers in a manner that is independent of both white noise and the signal level $\bar{S}_{OCT}$, we previously proposed a motility amplitude metric M according to [17]:

$$M = \sqrt{\frac{\Gamma(t_s) - \bar{S}_{OCT}^{\,2}}{\bar{S}_{OCT}^{\,2}}}\,. \tag{1}$$

Looking at Fig. 1a, we can see how M quantifies the motile scatterer contribution, and is normalized by $\bar{S}_{OCT}{}^2$ such that it is a unitless number; the final square root makes M linear with the OCT signal. This choice of normalization was found to impart depth-invariance to M, even under significant OCT signal roll-off [17]. Here, the value of M is reported for each of the spheroid conditions displayed in Fig. 1b, which ranges from a background level of 0.12 for the fixed spheroid, to a high value of 0.34 for the control spheroid. Thus, while long-time correlations are quantified by the time-averaged OCT signal $\bar{S}_{OCT}$, M is an excellent proxy for the relative contribution of short-time ($t_s < t_m < t_{total}$) correlations in dynamic OCT data. As such, here we focus efforts on compressive sampling toward accurately estimating "motility images" rendered by M.

2.2. Proposed method of compressive sampling

Our goal is to collect fewer samples of S_{OCT} while maintaining the ability to accurately estimate the short-time correlation, $\Gamma(t_s)$, and the long-time correlation, $\Gamma\left(t_{total}\right) \approx \bar{S}_{OCT}{}^2$, which subsequently enables computation of M according to Eq. (1). Given the unbiased, discrete autocorrelation of S_{OCT}:

$$\Gamma\left(j \cdot t_s\right) = \frac{1}{N-j} \sum_{i=0}^{N-j-1} S_{OCT}\left((i+j)t_s\right) S_{OCT}\left(i \cdot t_s\right), \tag{2}$$

where N is the number of samples, we write $\Gamma(t_s)$ as:

$$\Gamma\left(t_s\right) = \frac{1}{N-1} \sum_{i=0}^{N-2} S_{OCT}\left((i+1)t_s\right) S_{OCT}\left(i \cdot t_s\right). \tag{3}$$

Given a maximum available sampling rate of the OCT system $1 / t_s$, we see that it is necessary to collect adjacent pairs of S_{OCT} samples, $(i \cdot t_s, (i+1)t_s)$, to compute $\Gamma(t_s)$. We might consider simply collecting fewer samples N, however, that would decrease t_{total}, lead to a smaller time window for t_m of the motile processes, and rapidly break down the approximation $\Gamma\left(t_{total}\right) \approx \bar{S}_{OCT}{}^2$ (which, based on simulations presented below, is likely to already be a limiting factor in our experiments). If, on the other hand, we increase the sampling time t_s while keeping t_{total} constant, we similarly narrow the available window for t_m on the short time side, and potentially lose motility signal amplitude for portions of the signal that decay faster than the longer t_s. This latter scenario we will call the "uniform compressive sampling" (UCS) method, where t_s is increased by some integer compression ratio, *e.g.*, $t_s \rightarrow 2t_s$, $4t_s$, or $8t_s$ (and $N \rightarrow N/2$, $N/4$, or $N/8$) for 2-fold, 4-fold, or 8-fold compression, respectively. In the UCS method, the expression of Eq. (3) is used to compute $\Gamma(t_s)$, and the mean of all samples is computed to estimate $\bar{S}_{OCT}$.

Instead of UCS, here we propose a non-uniform (NUCS) method that avoids narrowing the window of t_m. This is accomplished by collecting adjacent pairs of samples (separated only by t_s) with an appropriate intervening dead time. Given a desired compression ratio r, we write the sampling scheme as:

$$i = 0, 1, 2r, 2r+1, 4r, 4r+1, 6r, 6r+1 \ldots \tag{4}$$

For example, to achieve a compression ratio of r=4, the signal would be sampled at times $i \cdot t_s$, where i = (1,2,9,10,17,18,…). In the NUCS method, $\Gamma(t_s)$ is then computed by multiplying just the adjacent pairs of samples according to:

$$\Gamma\left(t_s\right) = \frac{1}{N'} \sum_{i=0,2r,4r,\ldots}^{N-2} S_{OCT}\left((i+1)t_s\right) S_{OCT}\left(i \cdot t_s\right), \tag{5}$$

where N is the number of samples if the system were uncompressed (*i.e.*, $N = (t_{total} / t_s) + 1$), and N' is the number of compressively sampled pairs (which $\approx N/2r$ with rounding). As with the UCS method, $\bar{S}_{OCT}$ in NUCS is estimated by computing the mean of all available samples. We note that, while not used in this paper, if one wished to estimate the variance of $\Gamma(t_s)$, one would employ the finite population correction, since $\Gamma(t_s)$ is sampled without replacement.

2.3. Monte Carlo simulations

In order to quantify the impact of NUCS on extracting motility data from OCT images, we developed a simple simulation model to capture the additive contributions of white noise, motile scatterers, and stationary scatterers. The OCT signal sampled at N evenly spaced time points, t_i, $i = 0 \ldots N\text{-}1$, is written as follows:

$$S_{OCT}(t_i) = c_n f_n(t_i) + c_m f_m(t_i) + 1, \tag{6}$$

where f_n is the contribution of white noise, f_m is the contribution of motile scatterers with a persistence (memory) time of p sampling points, and an offset of 1 represents the stationary scatterers. The weights c_m and c_n are used to adjust the contributions of motile scatterers and white noise, respectively, relative to the offset. (For simplicity, here we assume noise is purely additive and ignore contributions from multiplicative noise, the latter of which was found to have negligible impact at the noise levels explored in this paper). The white noise and motility functions are computed according to

$$f_n(t_i) \sim N(0,1), \tag{7}$$

and

$$f_m(t_i) = \sqrt{p}\left(\frac{1}{p}\sum_{j=i}^{i+p-1} X(t_j)\right); \qquad X(t_j) \sim N(0,1), \tag{8}$$

respectively, where $N(0,1)$ denotes a zero-mean normal distribution with a variance of 1. While the white noise is represented by a purely random distribution, the motile scatterers are represented by a function with memory that is imparted by taking a moving average over a time window of $p \cdot t_s$. An additional weight of $\sqrt{p}$ is introduced to keep the variance of f_m constant at 1. While there are other models for memory that could be used, such as diffusion, for the purposes of this study we do not wish to presume a particular physical model for the dynamic process.

Importantly, the model of Eq. (6) – (8) allows us to test the impact of varying contributions of white noise, motile scatterers, and stationary scatterers. Because the variances of the noise and motile scatterer contributions are scaled by c_n^2 and c_m^2 respectively, and $\bar{S}_{OCT}$ is given by the offset which is equal to 1, we expect that:

$$\Gamma(0) = c_n^{\,2} + c_m^{\,2} + 1, \tag{9}$$

$$\Gamma(t_s) \approx c_m^{\,2} + 1, \tag{10}$$

$$\Gamma(t_{total}) \approx \bar{S}_{OCT}^{\,2} = 1, \tag{11}$$

and thus M according to Eq. (1) is approximately equal to c_m.

2.4 Mammary spheroid 3D cultures

3D cell cultures were prepared as described previously in [19]. The data analyzed and compressively sampled here are a subset of those initially reported in that paper. Briefly, the spheroids studied here were comprised of MCF10DCIS.com cells, a pre-malignant human mammary epithelial cell line that forms ductal carcinoma *in situ*- (DCIS-) like lesions in

xenograft models [25]. Cells were initially cultured in 2D until reaching 70% confluency, then seeded in 3D at a density of 30,000 cells / cm^3 into artificial extracellular matrix comprised of 1:1 collagen I:Matrigel (BD Biosciences) at a final collagen I concentration of 1 mg/mL. The MCF10DCIS.com cells were subsequently grown for 10 days to allow for spheroid formation in the 3D cultures. At this time, blebbistatin, an inhibitor of the motor protein myosin II, was introduced into the cell media at either 0, 25μM, or 50μM concentration. OCT imaging was performed on cultures immediately prior to blebbistatin exposure, and subsequently at 1 hour, 24 hours, 48 hours, and 6 days post exposure, for a total of 15 unique dose and time conditions.

For images of fixed spheroids reported in Fig. 1, 3D cultures were prepared as above, grown for 19 days, then fixed with formalin.

2.5 OCT imaging and post-processing

3D organoid cultures were imaged by a custom spectral-domain optical coherence tomography (SD-OCT) system described in detail previously [26], using the methods specifically outlined in [19]. Briefly, the light source is a Ti:Sapphire laser with a central wavelength of 800 nm and bandwidth of 120 nm, providing a lateral and axial resolution of ~10 μm × 3 μm (in aqueous medium), respectively, with a sensitivity of ~108 dB. Polarization control was used such that the sample was illuminated with horizontally polarized light, and returned backscattered light was passed through a polarizer to select the co-polarized (horizontal) component; this is important since temporal dynamics in OCT may differ between co- and cross-polarized components [8]. Images were collected into 1000 × 1024 pixels over 3 mm × 1.5 mm (in aqueous medium) laterally and axially, respectively. The A-line rate was set to 2 kHz and the resulting frame rate (accounting for dead time between frames) was 0.89 Hz. A total of 300 B-mode images were collected and divided into 3 sets of $N = 100$ images each for independent analysis. As such, we expect this sampling condition to allow for detection of motile scatterers with fluctuations on time scales between $t_s = 1.12$s and $t_{total} = 112$s.

2.5.1 Experimental image post-processing

Raw spectral OCT data were converted to depth-resolved B-mode images via Fourier transformation using digital dispersion compensation and reference subtraction. The region of each visible spheroid was segmented with assistance by a custom script to semi-automate the process [27], with typically 1-4 spheroids per B-mode image set. M was computed at each pixel according to methods outlined in section 2.2. For uncompressed analyses, all $N = 100$ images were used, while for compressive sampling, a subset of images was selected as described above. Both NUCS and UCS methods were employed using compression ratios of 2, 4, 8, and 16, reducing the total number of samples for UCS to $N = 50$, 25, 13, and 7, respectively. With NUCS, the total number of samples was reduced to $2N' = 50$ (25 pairs), 26 (13 pairs), 14 (7 pairs), and 8 (4 pairs), respectively, via the method of Eq. (4). While the total number of retained samples is slightly better for many of the non-uniformly sampled sets, as will be shown below, the overall comparative performances show much larger trends than can be explained by these differences.

The accuracy of M estimation was evaluated on a pixel-by-pixel and spheroid-by-spheroid basis. The pixel-wise M reveals the spatial pattern of motility inside spheroids. In the pixel-wise M analysis, a spatial mean filter of 12 μm × 3 μm (4 × 2 pixels) window size (laterally and axially, respectively) was applied to uncompressed and compressed M images. Subsequent segmentation of the spheroid regions was used to produce pixel-wise scatter plots of compressed versus uncompressed M. Scatter plots were fitted to a regression line of the form $y = mx$ (no offset) and the slope m and correlation coefficient (Pearson's r) were computed. Spheroid-averaged M, computed by segmenting M images without any prior mean filtering, were used to track the motility response of spheroids to different culture conditions (toxicant dose and exposure time). M was computed uncompressed and via NUCS and UCS with 4- and 8-fold compression. Spheroid-averaged scatter plots comparing compressed to uncompressed

M were analyzed as before. Then, *M* data grouped by culture condition were analyzed in parallel for each method (uncompressed, and 4-fold and 8-fold NUCS and UCS), performing a t-test (2-tailed, heteroscedastic) comparing *M* data of spheroids at each dose and time condition to the corresponding *M* data before exposure.

2.5.2 Simulation data processing

The Monte Carlo model described in 2.3 was employed to simulate the dynamic OCT signal collected within a pixel using settings chosen to match experimental conditions. As such, each simulation for a particular input of noise and motile scatterer weights c_n and c_m was comprised of time series of $N = 100$ points and repeated 6000 times (to approximate the average number of pixels within the spheroids in our study). *M* for each of the 6000 simulated time series was computed and averaged in the same way as for experimental OCT data, to produce the simulated spheroid-averaged *M*.

3. Results and Discussion

3.1 Simulations of compressive sampling

The model of Eq. (6) was employed to systematically investigate the impact of the proposed NUCS method on measurements of *M* spatially averaged over a typical spheroid size. Fig. 2A shows how *M* is varied in this model by modifying the weight of the motility function, c_m, under varying levels of noise, c_n. As expected, *M* nearly equals c_m and increases monotonically with it. There is a threshold minimum value of *M* as c_m approaches zero that increases with increasing noise, which is important to note when interpreting *M* from samples with predominantly stationary scatterers or regions with low SNR. The fact that *M* is somewhat smaller than c_m even for large input values is due to the approximative nature of Eq. (10) and (11), *i.e.*, that some of the motile scatterer contribution decorrelates before t_s, and some of it does not decorrelate by t_{total}, giving rise to an under-estimate of $\Gamma(t_s)$ and over-estimate of $\bar{S}_{OCT}{}^2$, both of which reduce *M* via Eq. (1). The amount of these errors depends upon the exact choice of the memory time. For the simulations of Fig. 2 we chose a memory time of $t_m = 20\ t_s$ ($p = 20$) and total number of samples $N = 100$ to recapitulate the relative values of t_m, t_s and t_{total} in MEC spheroid experiments. Notably, for p=20, error in *M* arising from $\bar{S}_{OCT}{}^2$ is significantly larger than that from $\Gamma(t_s)$, although we were unable to confirm this trend in the experimental data reported below as we lacked ground-truth values of *M*.

It is interesting to note that the reduction of *M* relative to c_m could be corrected if one knew *a priori* the functional form of the autocorrelation decay curve, such as an inverse exponential in the case of diffusing scatterers. However, a diffusion model, which would be consistent with a Lorentzian power spectrum, is inconsistent with power spectra from MEC spheroids in other experiments [17]. Therefore, such an approach may not be possible for the highly complex MEC spheroids of this study.

Figures 2B and 2C illustrate the impact of uniform compressive sampling (*i.e.* by simply increasing t_s), and by the proposed NUCS method of Eq. (4), respectively. Each point on the scatter plots represents a given simulation where *M* was computed either from the full data (uncompressed), or by appropriately downsampling the data (compressed). We can clearly see a rapid degradation in *M* estimation with increasing compression ratio for the uniform sampling method, where *M* above ~0.1 is significantly under-estimated for compression ratios of 4 and above (slope $\leq$ 0.84). This is expected because t_s increases with increasing compression, resulting in increased decorrelation by the motile scatterers (breakdown of Eq. (10), which lowers the overall *M* value). In contrast, for the proposed non-uniform sampling method, *M* is well reproduced at up to 8-fold compression, where it keeps ~94% of its baseline value. With NUCS, we found that breakdown of Eq. (11) (inaccurate estimation of $\bar{S}_{OCT}{}^2$) ultimately led to the reduced slope relative to the ideal $y = x$ line.

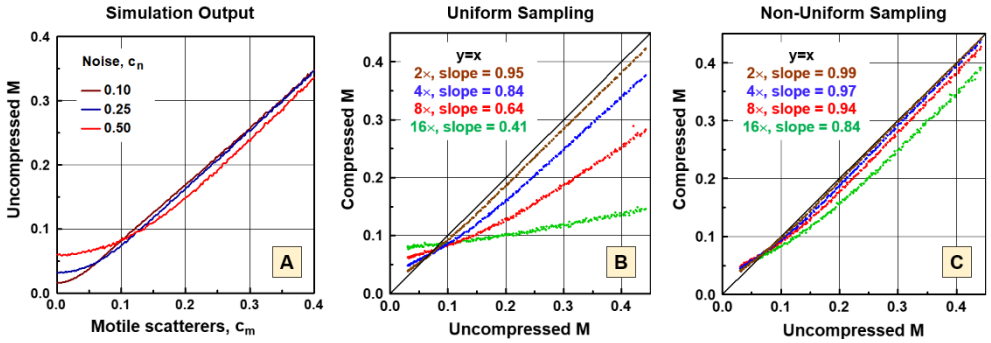

Fig. 2. Monte Carlo simulations of dynamic OCT signals using the model of Eq. (6). (A) Simulated measurements of M with varying contributions of motile scatterers (c_m) and noise (c_n). As noise increases, the background M level increases. (B, C) Scatter plots of simulated M measurements (compressed versus uncompressed) with uniform or non-uniform temporal sampling, respectively. While all conditions exhibited good correlation between compressed and uncompressed M, as the compression ratio increased, the slopes obtained by linear regression decreased from the ideal value of 1. Overall, the proposed method of non-uniform sampling exhibited superior performance, with a slope of 0.94 at 8-fold compression. In these simulations, c_m was varied from 0 to 0.5 and c_n was set to 0.25 to approximate typical spheroid data.

3.2 NUCS preserves spatial patterns of intracellular motility

Given the promising results of the simulations, we next explore how the proposed NUCS method performs on an existing dataset of MEC spheroids collected without compression, with UCS also performed as a point of comparison. Motility images, *i.e.*, spatial maps of M computed at each pixel and subsequently mean filtered over a resolution window, are computed for the two examples of live spheroids in Fig. 1. Motility images computed under varying levels of compression are displayed in Fig. 3, with the time-averaged OCT images ($\bar{S}_{OCT}$) displayed in grayscale for reference. As expected, we can qualitatively see that while $\bar{S}_{OCT}$ exhibits heavy attenuation with depth, the motility images do not suffer from signal roll-off. Importantly, consistent with the simulations, we see that the motility images using UCS decrease in contrast dramatically with increasing compression ratio, while NUCS maintains both the contrast and spatial pattern of M up to 8-fold compression. Particularly telling is a closeup of one spheroid in the blebbistatin-treated sample with a complex structure that is maintained after NUCS. These findings are favorable for future investigations into spatial patterns of motility within spheroids as related to drug or toxicant exposures and associated cell responses such as cancer metastasis.

To quantify the accuracy of NUCS, the right column of Fig. 3B shows pixel-by-pixel scatter plots of compressed versus uncompressed M within a region of interest inside a control spheroid. Consistent with simulations, the slope of the regression line decreases with increasing compression from 0.985 (2-fold) to 0.913 (8-fold). The spread of the data, however, appears qualitatively larger than in simulations, an effect which can be quantified by Pearson's r. We found that Pearson's r decreases with increasing compression from 0.89 (2-fold) to 0.66 (8-fold). To show how the NUCS method performs across the entire data set, which represents a variety of dose and culture time conditions, we tabulated the slope and Pearson's r computed from pixels within each spheroid, then averaged across each unique culture condition. Overall, the findings are similar to those represented in Fig. 3, with little change in accuracy as a function of culture condition.

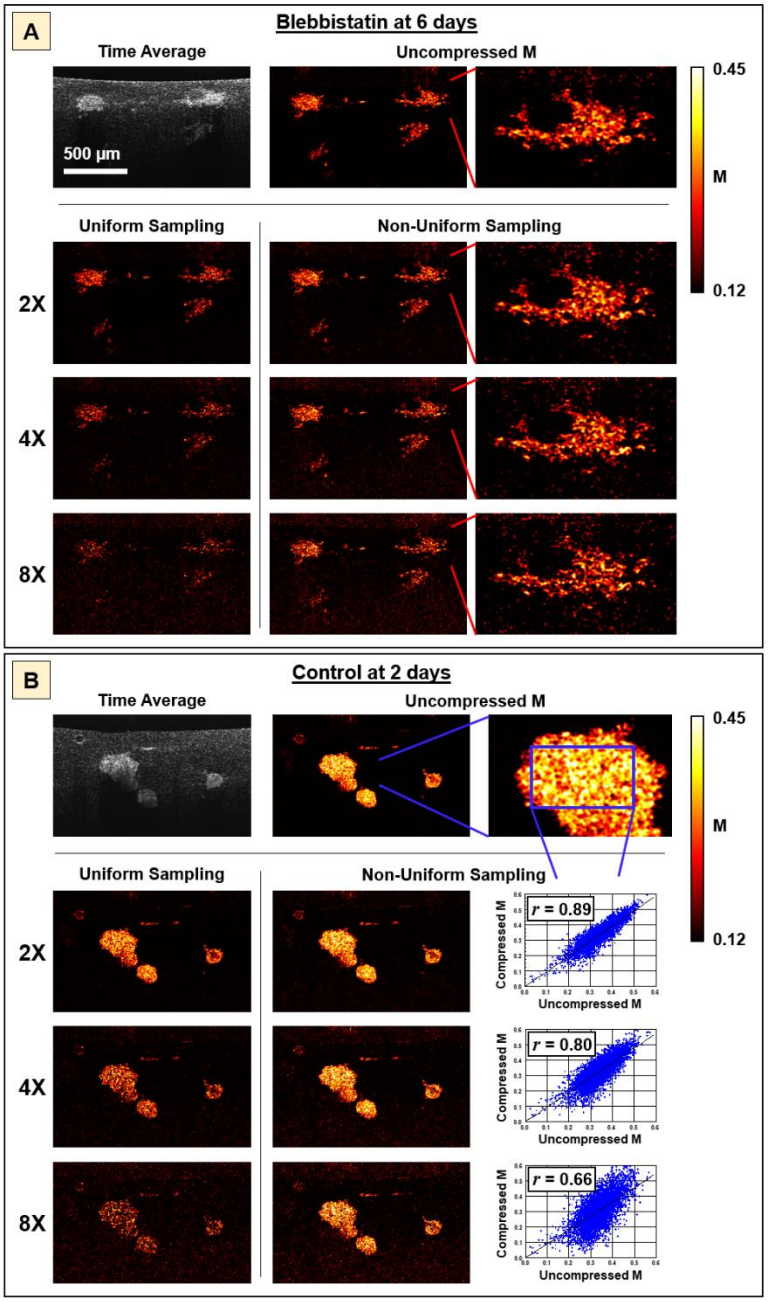

Fig. 3. (A,B) Effects of compressive sampling on motility imaging of weakly motile spheroids (blebbistatin treated) and highly motile spheroids (control), respectively. Top row: Time averaged OCT images and corresponding uncompressed motility images. Subsequent rows show the effects of increased compression ratio (2×, 4×, and 8×) with either uniformly sampled data (left) or the proposed NUCS method (middle) for each condition. (A, right column): Closeup of a blebbistatin-treated spheroid with varying levels of NUCS, showing how the structure is preserved. (B, right column): Pixel-by-pixel scatter plots of non-uniformly compressively sampled vs. uncompressed *M* for a control spheroid demonstrate a good-to-moderate correlation *r* with increasing compression.

3.3 NUCS preserves results of hypothesis testing

Because temporal dynamics of *in vitro* cell cultures imaged by OCT are increasingly used to infer responses of cells to a variety of perturbations, it is important to ensure that compressively sampled OCT does not alter the conclusions drawn from such experiments. Here we tested the veracity of the proposed NUCS method to assess the significance of changes in MEC spheroid intracellular motility in response to blebbistatin exposure. A data set of MEC spheroids imaged in triplicate with OCT for a total n=1428 was used for this purpose. Previously, spheroid-averaged M were computed and shown to be significantly different before and after exposure for certain blebbistatin dose and time points [19]. Here we non-uniformly downsampled these data according to Eq. (4), computed M according to Eq. (5), and performed the same hypothesis tests with the compressed M values to look for any differences in statistical significance. Results are summarized in Fig. 4.

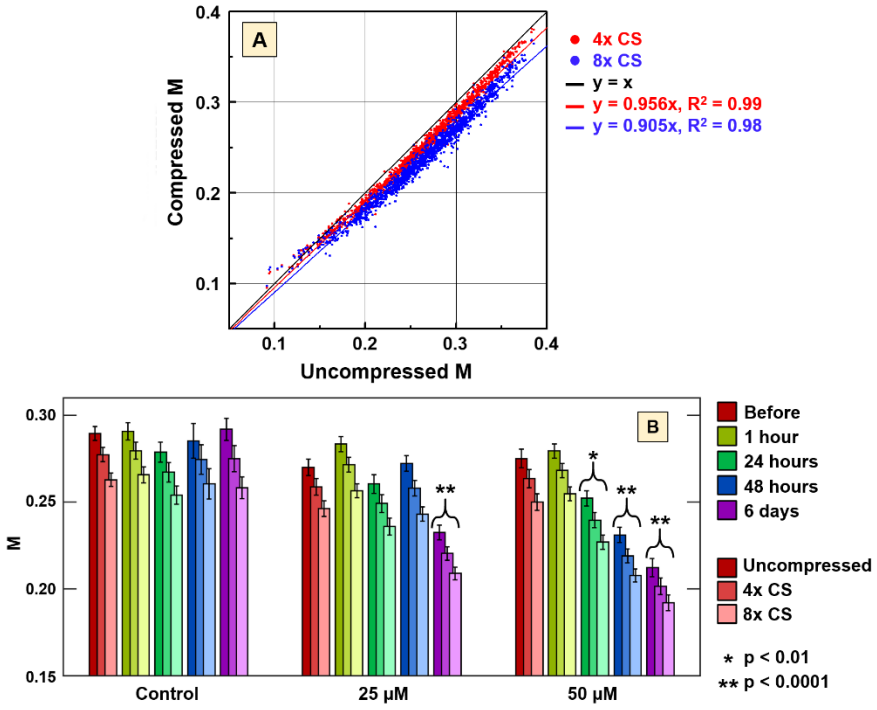

Fig. 4. (A) Spheroid-by-spheroid scatter plot of 4× and 8× non-uniformly compressively sampled versus uncompressed M over all blebbistatin concentrations and time points (n=1428). Best-fit lines indicate good linearity with a small reduction in the slope from the ideal y=x line as the compression level is increased from 4× to 8×. (B) Dose- and time-dependent M (mean ± std. err) of spheroids exposed to blebbistatin under varying compression levels. Hypothesis testing (2-tailed t-test compared to corresponding before values) indicates similar significance levels when performed on compressed or uncompressed data.

A spheroid-to-spheroid scatter plot of non-uniformly compressively sampled versus uncompressed M across this data set is displayed in Fig. 4A. Similar to pixel-to-pixel data, the regression line slope decreases with increasing compression. However, the spread of data is significantly smaller for spheroid-averaged data due to increased spatial averaging, exhibiting high correlations (R^2 = 0.99 and 0.98 for 4- and 8-fold compression, respectively). The results also display the same trends as those of the simulations displayed in Fig. 2C. Fig. 4B shows the resulting condition-averaged M for each dose and time point under each compression level. As shown, the overall M values become smaller with higher compression (as evidenced by the decrease in the slope of the scatter plot regression line from the ideal value of 1 to 0.956 and

0.905 for 4- and 8-fold compression, respectively). However, because the *M* values within each compression level track together (*i.e*. have high correlation), the associated *p*-values remain largely unchanged, and the same results when examining *p*-values relative to significance levels are obtained (see asterisks on the bar chart in Fig. 4b).

4. Conclusion

A method is proposed for temporal compressive sampling with OCT by non-uniformly sampling the OCT data in time to capture short- and long-term correlations within the sample. Compared to uniformly sampling data in time, the NUCS method exhibits dramatically improved accuracy, both in simulation and on experimental data, for estimating the relative amplitude of fluctuations imparted by motile scatterers. Here, motile scatterers are defined as those that cause OCT signal fluctuations at time scales longer than the sampling time t_s, and shorter than the total imaging time t_{total}. When applying this technique to different applications, a careful choice of both t_s and t_{total} is first needed to define the temporal window over which motile scatterers are contrasted by this technique.

Our study shows that the data reduction levels achievable by NUCS are dramatic, with up to 8-fold compression on a data set with 100 time samples preserving both the spatial pattern of intracellular motility in MEC spheroids, and statistical significance of cellular responses to blebbistatin treatment. This constitutes a leap forward in our capability to employ OCT as a non-invasive tool to study dynamic processes, which is currently limited by both scanning times and data overhead. For example, one could implement the sampling strategy of Eq. (6) by breaking a volume up into sub-volumes comprised of a set of *r* adjacent B-mode frames (where *r* is the compression ratio), cycling through each elevational position while pausing long enough at each to collect sequential frames, and returning back to each position in the same sequence over the desired total number of samples. Current commercially available OCT systems can be programmed to scan with such patterns. The concomitant reduction in data overhead is also crucial to reduce a typical OCT image stack for one cross-section in time from ~100 MB to ~13 MB in size, which is significant when multiplied over the number of frames in a volume for (3+1)D imaging. These enhancements will enable new applications in OCT-based sensing of 3D cell cultures in particular, where high-throughput imaging is desired for drug discovery and toxicant exposure applications. Laser speckle contrast imaging, which similarly involves assessment of autocovariances of speckle fluctuations from biological media [28], may also benefit from the methods proposed here. The NUCS method may be broadly applicable to study dynamic processes in complex biological or non-biological systems exhibiting temporal correlations on different time scales.

Funding. National Institutes of Health (R01ES032730, R21CA179204, P30ES10126).

Acknowledgments. None.

Disclosures. The authors declare no conflicts of interest.

Data availability. Underlying, raw image data are not publicly available at this time but may be obtained from the authors upon reasonable request.

References

1. D. A. Boas, K. K. Bizheva, and A. M. Siegel, "Using dynamic low-coherence interferometry to image Brownian motion within highly scattering media," Opt. Lett. **23**, 319-321 (1998).
2. J. A. Izatt, M. D. Kulkarni, S. Yazdanfar, J. K. Barton, and A. J. Welch, "In vivo bidirectional color Doppler flow imaging of picoliter blood volumes using optical coherence tomography," Opt Lett **22**, 1439-1441 (1997).
3. G. Farhat, A. Mariampillai, V. X. D. Yang, G. J. Czarnota, and M. C. Kolios, "Detecting apoptosis using dynamic light scattering with optical coherence tomography," J Biomed Opt **16**, 070505-070505 (2011).
4. Y. Jia, O. Tan, J. Tokayer, B. Potsaid, Y. Wang, J. J. Liu, M. F. Kraus, H. Subhash, J. G. Fujimoto, and J. Hornegger, "Split-spectrum amplitude-decorrelation angiography with optical coherence tomography," Opt Express **20**, 4710-4725 (2012).

5. D. D. Nolte, R. An, J. Turek, and K. Jeong, "Tissue dynamics spectroscopy for phenotypic profiling of drug effects in three-dimensional culture," Biomed. Opt. Express **3**, 2825-2841 (2012).
6. A. L. Oldenburg, R. K. Chhetri, D. B. Hill, and B. Button, "Monitoring airway mucus flow and ciliary activity with optical coherence tomography," Biomed. Opt. Express **3**, 1978-1992 (2012).
7. K. K. Chu, C. Unglert, T. N. Ford, D. Cui, R. W. Carruth, K. Singh, L. Liu, S. E. Birket, G. M. Solomon, and S. M. Rowe, "In vivo imaging of airway cilia and mucus clearance with micro-optical coherence tomography," Biomed Opt Express **7**, 2494-2505 (2016).
8. R. K. Chhetri, R. L. Blackmon, W.-C. Wu, D. B. Hill, B. Button, P. Casbas-Hernandez, M. A. Troester, J. B. Tracy, and A. L. Oldenburg, "Probing biological nanotopology via diffusion of weakly constrained plasmonic nanorods with optical coherence tomography," Proceedings of the National Academy of Sciences **111**, E4289-E4297 (2014).
9. B. Baumann, B. Potsaid, M. F. Kraus, J. J. Liu, D. Huang, J. Hornegger, A. E. Cable, J. S. Duker, and J. G. Fujimoto, "Total retinal blood flow measurement with ultrahigh speed swept source/Fourier domain OCT," Biomed Opt Express **2**, 1539-1552 (2011).
10. M. Münter, M. Pieper, T. Kohlfaerber, E. Bodenstorfer, M. Ahrens, C. Winter, R. Huber, P. König, G. Hüttmann, and H. Schulz-Hildebrandt, "Microscopic optical coherence tomography (mOCT) at 600 kHz for 4D volumetric imaging and dynamic contrast," Biomed Opt Express **12**, 6024-6039 (2021).
11. J. Scholler, K. Groux, O. Goureau, J.-A. Sahel, M. Fink, S. Reichman, C. Boccara, and K. Grieve, "Dynamic full-field optical coherence tomography: 3D live-imaging of retinal organoids," Light: Science & Applications **9**, 1-9 (2020).
12. Z. Li, R. An, W. M. Swetzig, M. Kanis, N. Nwani, J. Turek, D. Matei, and D. Nolte, "Intracellular optical doppler phenotypes of chemosensitivity in human epithelial ovarian cancer," Scientific reports **10**, 1-10 (2020).
13. X. Yu, A. M. Fuller, R. Blackmon, M. A. Troester, and A. L. Oldenburg, "Quantification of The Effect of Toxicants on the Intracellular Kinetic Energy and Cross-Sectional Area of Mammary Epithelial Organoids by OCT Fluctuation Spectroscopy," Toxicological Sciences (2017).
14. X. Liu, and J. U. Kang, "Compressive SD-OCT: the application of compressed sensing in spectral domain optical coherence tomography," Opt Express **18**, 22010-22019 (2010).
15. I. A. El-Sadek, A. Miyazawa, L. T.-W. Shen, S. Makita, P. Mukherjee, A. Lichtenegger, S. Matsusaka, and Y. Yasuno, "Three-dimensional dynamics optical coherence tomography for tumor spheroid evaluation," Biomed Opt Express **12**, 6844-6863 (2021).
16. N. Mohan, and B. Vakoc, "Principal-component-analysis-based estimation of blood flow velocities using optical coherence tomography intensity signals," Opt Lett **36**, 2068-2070 (2011).
17. A. L. Oldenburg, X. Yu, T. Gilliss, O. Alabi, R. M. Taylor, and M. A. Troester, "Inverse-power-law behavior of cellular motility reveals stromal–epithelial cell interactions in 3D co-culture by OCT fluctuation spectroscopy," Optica **2**, 877-885 (2015).
18. J. C. McIntosh, L. Yang, T. Wang, H. Zhou, M. R. Lockett, and A. L. Oldenburg, "Tracking the invasion of breast cancer cells in paper-based 3D cultures by OCT motility analysis," Biomed Opt Express **11**, 3181-3194 (2020).
19. L. Yang, X. Yu, A. M. Fuller, M. A. Troester, and A. L. Oldenburg, "Characterizing optical coherence tomography speckle fluctuation spectra of mammary organoids during suppression of intracellular motility," Quantitative Imaging in Medicine and Surgery **10**, 76 (2020).
20. B. J. Blackburn, S. Gu, M. R. Ford, V. de Stefano, M. W. Jenkins, W. J. Dupps, and A. M. Rollins, "Noninvasive assessment of corneal crosslinking with phase-decorrelation optical coherence tomography," Invest Ophthalmol Vis Sci **60**, 41-51 (2019).
21. Z. Xu, H. Zhu, and H. Wang, "Segmentation of the urothelium in optical coherence tomography images with dynamic contrast," J Biomed Opt **26**, 086002 (2021).
22. J. Kalkman, R. Sprik, and T. G. van Leeuwen, "Path-Length-Resolved Diffusive Particle Dynamics in Spectral-Domain Optical Coherence Tomography," Phys Rev Lett **105**, 198302 (2010).
23. N. Uribe-Patarroyo, A. L. Post, S. Ruiz-Lopera, D. J. Faber, and B. E. Bouma, "Noise and bias in optical coherence tomography intensity signal decorrelation," OSA Continuum **3**, 709-741 (2020).
24. A. L. Oldenburg, R. K. Chhetri, J. M. Cooper, W.-C. Wu, M. A. Troester, and J. B. Tracy, "Motility-, autocorrelation-, and polarization-sensitive optical coherence tomography discriminates cells and gold nanorods within 3D tissue cultures," Opt Lett **38**, 2923-2926 (2013).
25. F. R. Miller, S. J. Santner, L. Tait, and P. J. Dawson, "MCF10DCIS.com xenograft model of human comedo ductal carcinoma in situ," J Natl Cancer Inst **92**, 1185-1186 (2000).
26. R. K. Chhetri, K. A. Kozek, A. C. Johnston-Peck, J. B. Tracy, and A. L. Oldenburg, "Imaging three-dimensional rotational diffusion of plasmon resonant gold nanorods using polarization-sensitive optical coherence tomography," Phys Rev E Stat Nonlin Soft Matter Phys **83**, 040903 (2011).
27. A. M. Fuller, L. Yang, A. M. Hamilton, J. R. Pirone, A. L. Oldenburg, and M. A. Troester, "Epithelial p53 Status Modifies Stromal-Epithelial Interactions During Basal-Like Breast Carcinogenesis," J Mammary Gland Biol **26**, 89-99 (2021).
28. A. B. David, and K. D. Andrew, "Laser speckle contrast imaging in biomedical optics," J Biomed Opt **15**, 1-12 (2010).